



HAL
open science

Determination of strain path during martensitic transformation in materials with two possible transformation orientation relationships from variant self-organization

Hai-Le Yan, Zhang Yu-Dong, Claude Esling, Xiang Zhao, Liang Zuo

► **To cite this version:**

Hai-Le Yan, Zhang Yu-Dong, Claude Esling, Xiang Zhao, Liang Zuo. Determination of strain path during martensitic transformation in materials with two possible transformation orientation relationships from variant self-organization. *Acta Materialia*, 2021, 202, pp.112-123. 10.1016/j.actamat.2020.10.054 . hal-03079277

HAL Id: hal-03079277

<https://hal.science/hal-03079277>

Submitted on 17 Dec 2020

HAL is a multi-disciplinary open access archive for the deposit and dissemination of scientific research documents, whether they are published or not. The documents may come from teaching and research institutions in France or abroad, or from public or private research centers.

L'archive ouverte pluridisciplinaire **HAL**, est destinée au dépôt et à la diffusion de documents scientifiques de niveau recherche, publiés ou non, émanant des établissements d'enseignement et de recherche français ou étrangers, des laboratoires publics ou privés.

**Determination of strain path during martensitic transformation in
materials with two possible transformation orientation
relationships from variant self-organization**

Hai-Le Yan¹, Yudong Zhang^{2,3,*}, Claude Esling^{2,3}, Xiang Zhao^{1,*}, Liang Zuo¹

¹*Key Laboratory for Anisotropy and Texture of Materials (Ministry of Education), School of
Material Science and Engineering, Northeastern University, Shenyang 110819, China*

²*Université de Lorraine, CNRS, Arts et Métiers ParisTech, LEM3, F-57000 Metz, France*

³*Laboratory of Excellence on Design of Alloy Metals for low-mAss Structures (DAMAS),
Université de Lorraine, F-57070, Metz, France*

*Corresponding authors:

yudong.zhang@univ-lorraine.fr; zhaox@mail.neu.edu.cn

Abstract

Determination of strain path across martensitic transformation in materials with two transformation orientation relationships (ORs) is challenging due to the temporal and spatial limitation of the modern techniques. In this work, an analyzing strategy, *i.e.*, the determination of transformation path *via* the variant organization feature of martensite, was suggested and applied for the Ni–Mn-based alloys as an example, based on the consideration that the different crystallographic symmetries of transformation systems will result in distinct organizations of martensite variants. For the selected Ni–Mn-based alloys, the orientation examination revealed that both the K–S and the Pitsch OR are respected. Further analyses in terms of the strain and stress compatibility condition and the minimum energy criteria showed that, theoretically, the K–S path produces 2 variants as a self-accommodated variant group, whereas the Pitsch path produces 4 variants as a self-accommodated variant group. Compared with the experimental results, the Pitsch path is the energetically favorable transformation path and actually occurs in stress-free austenite of the Ni–Mn based alloys. The significance of this work is multi-fold. It first resolves the long puzzling issue of transformation strain path of Ni–Mn-based alloys. Moreover, the analyzing scheme can be generalized to determine the transformation characters for martensitic transformation in other systems with multiple possible transformation orientation relationships.

Keywords: martensitic transformation; orientation relationship; transformation strain path; EBSD; crystallography

1. Introduction

Martensitic transformation lies at the origin of fruitful functionalities of the Ni–Mn-based alloys, such as magnetic shape memory effect [1-3], multicaloric effects [4-7], exchange bias [8], magnetoresistance [9, 10] and superelasticity [11-13]. The energy efficiency of these functions is closely related to the lattice distortion across the structural transition. Therefore, knowledge of the distortion process of martensitic transformation is crucial for materials design aiming at maximizing functionalities at the lowest energy consumption. Among various factors concerning the phase transformation, the transformation strain path is one of the most important factors that possesses both practical importance and theoretical significance [14]. In reality, the transformation strain path is closely related to the resistance of the structural transition, thus, it could play a decisive role in the hysteresis that deteriorates the functionality of the alloys [15, 16]. Solid knowledge on this issue is imperative for application purposes and also crucial for theoretical study or simulation of the phase transformation process, such as phase-field simulations and, in the more general sense, for the further development of martensitic transformation models.

In this regard, the study on the transformation strain path has been frequently conducted both theoretically and experimentally. In theoretical analyses, the Bain strain path $\{001\}_A$ $\langle 010 \rangle_A$ that results in the Bain orientation relationship (OR) between the parent and the product phase was first proposed as the transformation strain path to describe the structural transition for the Ni–Mn-based alloys [17-23]. It has been widely used to evaluate the lattice stability and/or to explore novel alloy compositions by the first-principles calculations [18]. The Bain strain path is also convenient to describe several materials properties, such as the energy of twin

interface and the magnetocrystalline anisotropy [24, 25]. However, in many materials, the Bain strain is not the true physical path of the transformation although it well explained the structure change. The Bain OR is seldom observed in the real transformations [26, 27].

To resolve a more realistic transformation path, the electronic instability of austenite based on the combined studies on the Fermi-surface nesting and the phonon dispersion relation [20-22] have been performed. The transformation path of $\{110\}_A \langle \bar{1}10 \rangle_A$ that results in the Pitsch OR between the parent austenite and the product martensite was proposed. Under this path, many puzzling phenomena for the Bain path, such as the incommensurateness of structural modulation [28] and the non-uniform displacement of shuffling plane [29], can be easily understood. It should be noted that theoretical results were obtained under ideal composition and temperature conditions that are far from the practical situation. Moreover, the transformation system of $\{111\}_A \langle 110 \rangle_A$ that results in the K-S OR between the two end phases [30] was also suggested for the structural transition of the Ni-Mn-based alloys [23].

Therefore, these theoretical propositions should be verified by experimental studies. However, the direct evidence of the transformation strain path by experiments is much more difficult, due to the temporal and spatial limitation of the atomic scaled characterization techniques, as the displacive martensitic transformation occurs at the speeds approaching that of the sound and the relative displacement of atoms is usually much smaller than the length of an atomic band [31, 32]. Moreover, the extreme sensibility of these materials to the stress-strain state makes the direct experimental observation of transformation path at the atomic scale even more difficult. To date, the investigation of the transformation path of the Ni-Mn-based alloys are mainly confined to the identification of the transformation OR. However, for the martensitic

transformation of Ni–Mn based alloys that produces modulated martensite, the Pitsch and the K–S OR are simultaneously satisfied [33-35], which bring about ambiguity to the transformation strain path. Moreover, the relation between the microstructural representation and the different possible transformation strain paths, *i.e.*, the organization of the martensite variants, has not been addressed. To this end, a top-down experimental strategy by examining microstructural and crystallographic features of the transformed microstructure combined with crystallographic decoding to determine the transformation strain path could be an effective approach.

Thus, in this work, we conducted a thorough investigation on the transformation strain path of the martensitic transformation of Ni–Mn–In alloys based on a combined study with microstructure characterization and crystallographic analysis by means of SEM electron backscattered diffraction (EBSD) technique. First, the possible transformation strain paths were evaluated by examining the crystallographic orientation relationship (OR) between austenite and martensite. For the various possible transformation paths, their correlated martensite variant combination configurations were then predicted under the strain and stress compatibility conditions and the minimum energy criterion for interface and elastic strain energies. By verifying the predicted microstructural features with the experimental evidence, the transformation strain path of the Ni–Mn-based alloys was determined. The result of this work has multi-folds of significance. It first resolves the long puzzling issue of transformation strain path of Ni–Mn-based alloys and provides solid experimental data for theoretical simulation of phase transformation processes using various novel models. Moreover, the analyzing scheme can be generalized to analyze the structural transition in the diffusional phase transformation of

many other alloy systems.

2. Experimental details

In this work, two alloys, one with a single martensite phase ($\text{Ni}_2\text{Mn}_{1.44}\text{In}_{0.56}$) [36] and the other with a mixed austenite and martensite ($\text{Ni}_{45}\text{Co}_5\text{Mn}_{36.8}\text{In}_{13.2}$) [37] at room temperature, were prepared by arc-melting technique using pure constituent elements Ni (99.97 wt.%), Co (99.9 wt.%), Mn (99.95 wt.%) and In (99.995 wt.%) under argon atmosphere in a water-cooled copper crucible. In order to achieve composition homogeneity, each ingot was remelted four times under electromagnetic stirring. The ingot was then remelted and injected into water chilled copper mold to obtain a dense cylindrical rod. The rod was first sealed in a quartz tube under argon atmosphere and then annealed at 1173 K for 24 hours and quenched in water. A rectangular parallelepiped sample with the sizes of $5 \times 5 \times 10 \text{ mm}^3$ was cut out of the middle of the cylindrical rod for microstructure and crystallographic orientation investigation. The inspected surface was first mechanically ground and then electrolytically polished with a solution of 20% nitric acid in methanol at room temperature. A field emission gun scanning electron microscope (Jeol JSM 6500 F) with an electron backscatter diffraction (EBSD) acquisition camera and the Aztec acquisition software package (Oxford Instruments) were used to perform the microstructural examination and crystallographic orientation measurement. The beam control mode was used with a step size of $0.125 \mu\text{m}$. To avoid the effect of free surface on martensitic transformation, the EBSD measurements were made on the freshly sectioned sample planes after the transformation had terminated in the bulk samples. No further thermal/mechanical treatment that may affect the self-organization of martensite variants [38] was performed.

3. Results and discussion

3.1 Martensite microstructure and transformation orientation relationship

In Figs. 1a and b, we show the typical SEM/EBSD micrographs of the coexisting austenite and martensite (measured with the $\text{Ni}_{45}\text{Co}_5\text{Mn}_{36.8}\text{In}_{13.2}$ sample) and the pure martensite phase (measured with the $\text{Ni}_2\text{Mn}_{1.44}\text{In}_{0.56}$ alloy) of the Ni–Mn–In based alloys. The alloy in Fig. 1a₁ is composed of austenite possessing cubic $L2_1$ structure [37] and martensite with a six-layer modulated (6M) monoclinic structure [36, 37]. Crystallographic orientation examination of the microstructure revealed that the two martensite domains (denoted G1 and G2) are located in one austenite grain. Each domain contains four orientation variants (denoted A, B, C and D), as shown in Fig. 1a₂. Misorientation analyses demonstrated that the four variants in one group are twin-related one another, *i.e.*, type-I (A: C and B: D), type-II (A: B and C: D) and compound twin (A: D and B: C), like the cases in some reported Ni–Mn-based alloys [39]. The interfaces between the variants coincide with their twinning plane K_1 [39]. It should be noted that the martensite variants shown in Fig. 1a were formed in the bulk material and in the interior of austenite grain rather than on the surface or near austenite grain boundaries. The influences of free surface and grain boundaries on the transformation strain path and the organization of the martensite variants were eliminated.

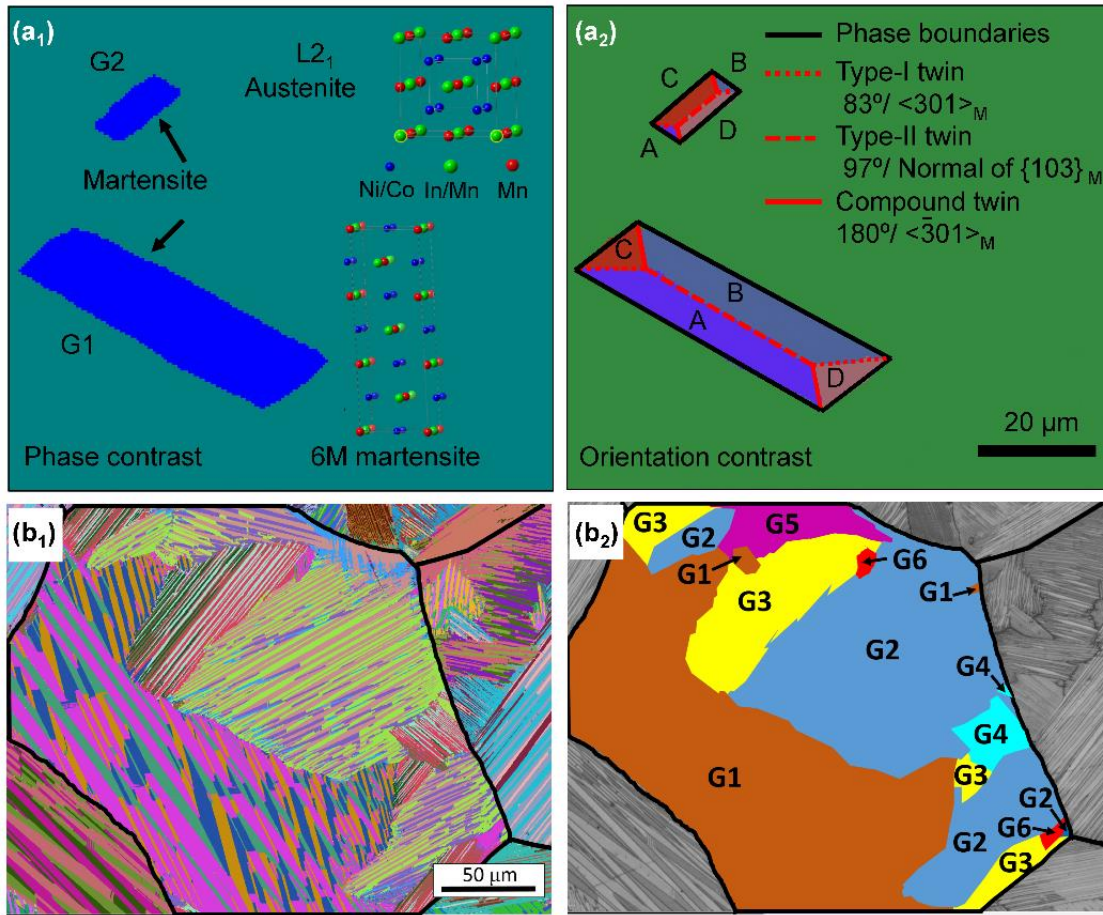


Fig. 1 Phase indexed (a₁) and orientation (a₂) micrographs of the dual-phase Ni₄₅Co₅Mn_{36.8}In_{13.2} alloy. The solid black lines indicate the phase boundaries between austenite and martensite. The red dotted, red dashed and red solid lines represent the type-I, type-II and compound twin interfaces. Crystallographic orientation (b₁) and band quality indexed (b₂) micrographs of the single martensite of the Ni₂Mn_{1.44}In_{0.56} alloy. The solid black lines represent the initial austenite grain boundaries. G1 to G6 indicate the distinct martensite groups.

The microstructure in Fig. 1b₁ revealed that when the martensitic transformation is complete, each initial austenite grain (as outlined with the black lines) transforms into several groups of the plate-shaped martensite variants. In each group, there are four martensite variants. The variants are inter-related with the above-determined three twin relations. This result indicates that each group with the plate-shaped martensite variants is originated from the variant group in Fig. 1a. Moreover, our experiments showed that one initial austenite grain can produce

maximum 6 orientation-independent groups of martensite variants, as shown in Fig. 1b₂, hence, in total, 24 martensite variants.

We now focus on the microstructure of Ni₄₅Co₅Mn_{36.8}In_{13.2} alloy (Fig. 1a) since the coexistence of austenite and martensite allows a direct verification of transformation ORs between the parent and the product phase using the ORs reported in the literature [17, 30, 40-42]. In Fig. 2, we display the possible ORs for the studied alloy, *i.e.*, the Bain (Fig. 2a), the Pitsch (Fig. 2b), the Kurdjumov–Sachs (K–S, Fig. 2c) and the Nishiyama–Wassermann (N–W, Fig. 2d) relations, which were selected based on the crystal structure features of the austenite and the martensite. In this work, the four ORs are discriminated with the angular differences between the theoretical (Δg_0^{OR}) and the experimental (Δg^{exp}) disorientations between the austenite and the martensite under each OR. The details of the calculations are described in Appendix A. The results expressed as the minimal deviation angle (ω) are listed in Table 1. We see that for the Bain OR, the deviation angles for all the variants in G1 and G2 groups (Fig. 1a) are the highest, larger than 3°, among the four ORs. A large deviation of the Bain OR was also reported in Ni–Mn–Ga [33], Ni–Mn–Sn [43] and Ni–Mn–Sb [35] alloys. Clearly, the Bain OR can be ruled out from being the suitable OR for the Ni–Mn-based alloys.

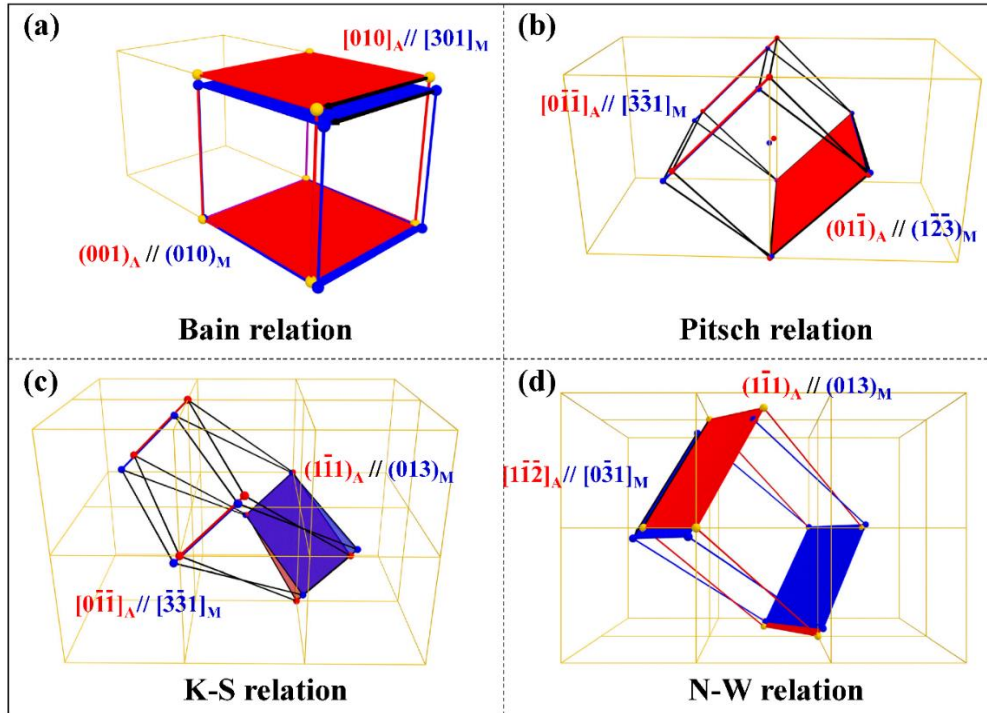


Fig. 2 Illustrations of lattice correspondences between the austenite and the martensite under the Bain (a), the Pitsch (b), the K–S (c) and the N–W (d) OR. The crystal lattices of the austenite and the martensite are indicated in red and blue, respectively. Subscripts “A” and “M” represent austenite and martensite, respectively.

Table 1 Angular deviation of the experimental disorientation (Δg^{exp}) from the theoretical disorientation (Δg_0^{OR}) between the austenite and the martensite under the Bain, the N–W, the K–S and the Pitsch relation.

ORs	Theoretical OR matrices expressed in austenite crystal coordinate system	Deviation of experimental OR from theoretical OR (°)					
		Variant group	Variant A	Variant B	Variant C	Variant D	Mean angle
Bain	$\begin{bmatrix} -0.6778 & 0 & 0.7353 \\ 0.7353 & 0 & 0.6778 \\ 0 & 1 & 0 \end{bmatrix}$	G1	3.28	3.90	4.33	3.40	3.73
		G2	3.63	4.08	4.08	3.14	3.73
N–W	$\begin{bmatrix} -0.6769 & 0.0529 & 0.7342 \\ 0.7355 & 0.0089 & 0.6775 \\ 0.0293 & 0.9986 & -0.0449 \end{bmatrix}$	G1	1.22	1.15	1.75	1.49	1.40
		G2	1.41	1.48	1.23	0.44	1.14
K–S	$\begin{bmatrix} -0.6859 & 0.0657 & 0.7248 \\ 0.7262 & -0.0032 & 0.6875 \\ 0.0475 & 0.9978 & -0.0455 \end{bmatrix}$	G1	0.65	0.78	0.57	0.88	0.72
		G2	0.50	0.50	0.77	0.90	0.67

Pitsch	$\begin{bmatrix} -0.0508 & -0.9978 & 0.0425 \\ -0.7290 & 0.0080 & -0.6844 \\ 0.6826 & -0.0657 & -0.7278 \end{bmatrix}$	G1	0.75	0.57	0.84	0.65	0.70
		G2	0.35	0.27	0.64	0.93	0.55

Apart from the Bain OR, the N–W OR also demonstrates a large mismatch (deviation angles $> 1^\circ$) for all the four martensite variants. Thus, the N–W path can also be excluded. Different from the above two ORs, we see from Table 1 that both the K–S and the Pitsch ORs possess the close deviation for all the variants (around 0.6°) and also the smallest deviations among the four ORs. Moreover, the values of the deviation for the two ORs are within the limit of the measurement error of the used EBSD technique ($\pm 0.5^\circ$). Thus, both the K–S and the Pitsch ORs were respected during the structural transformation.

In Fig. 3a, we illustrate the difference in geometry between the K–S and the Pitsch OR by comparing the martensite lattices under these two ORs. For simplicity, the average structure [44] of modulated martensite is used. We can see that the martensite lattices under the Pitsch (green) and the K–S (blue) ORs almost completely overlap. Calculations showed that the disorientation angle between these two lattices is as small as 0.44° . This means that the two ORs could be simultaneously satisfied in the present alloy system. A close examination of the OR systems (plane and direction) revealed that the two ORs share the common OR direction, *i.e.*, $[0\bar{1}\bar{1}]_A$ and $[\bar{3}\bar{3}1]_M$ but different OR planes, as shown in Fig. 3b. It is worth mentioning that such a dual OR phenomenon is not singular only for the present alloy. The same phenomenon has frequently been observed in many other Ni–Mn-based alloys possessing modulated martensite, such as the transformation to 7M modulated martensite in $\text{Ni}_{50}\text{Mn}_{30}\text{Ga}_{20}$ [33], to 5M modulated martensite in $\text{Ni}_{50}\text{Mn}_{28}\text{Ga}_{22}$ [34] and to 4O modulated martensite in $\text{Ni}_{50}\text{Mn}_{38}\text{Sb}_{12}$ [35].

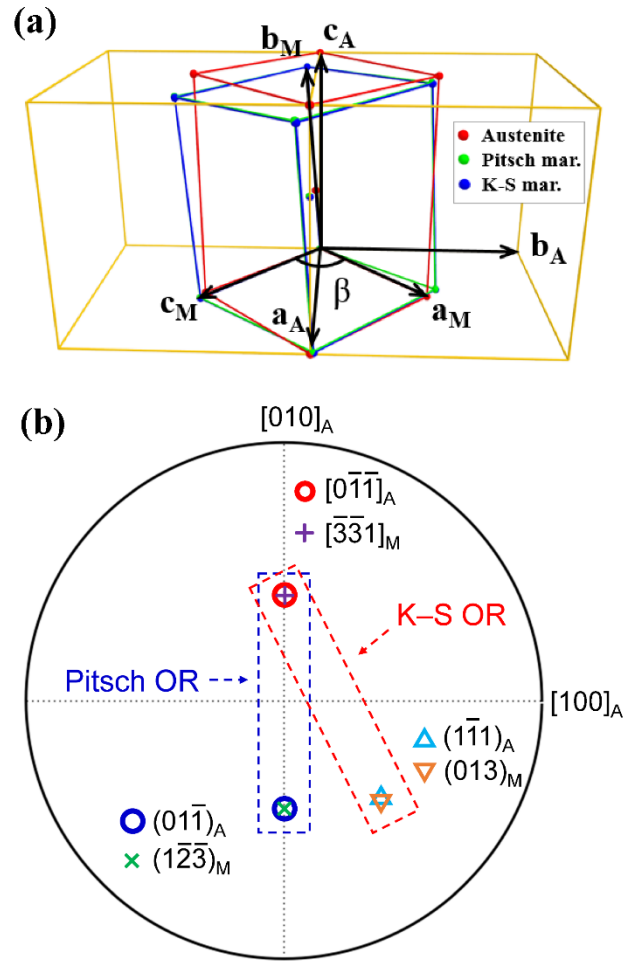


Fig. 3 (a) Orientations of martensite lattices under the K–S (blue) and the Pitsch (green) relation. (b) Stereographic projection of the OR planes and the OR directions for the K–S and the Pitsch OR in the lattice frame of austenite.

3.2 Transformation associated lattice deformation

With the determined possible ORs between the parent and the product phase, the lattice correspondences between the two phases can be established in the OR reference frame. Here, we define the reference system with three mutually perpendicular right-handed unit vectors, the first being perpendicular to both the OR direction and the normal of the OR plane, the second parallel to the OR direction and the third perpendicular to the OR plane, as shown in Fig. 4. Based on the minimum deformation criterion [45], the deformation gradient tensor (F) associated with the lattice deformation during phase transformation was calculated. F expressed

in the respective K–S and Pitsch OR reference frames are shown in Eqs. (1) and (2).

$$\mathbf{F}_{\text{K-S}}^{\text{OR}} = \begin{bmatrix} 1.0005 & 0 & -0.0021 \\ 0.0856 & 1.0001 & \mathbf{0.1002} \\ 0 & 0 & 0.9885 \end{bmatrix} \quad (1)$$

$$\mathbf{F}_{\text{Pitsch}}^{\text{OR}} = \begin{bmatrix} 0.9975025 & 0 & 0.0105 \\ -0.0121 & 1.0001 & \mathbf{-0.1312} \\ 0 & 0 & 0.9914 \end{bmatrix} \quad (2)$$

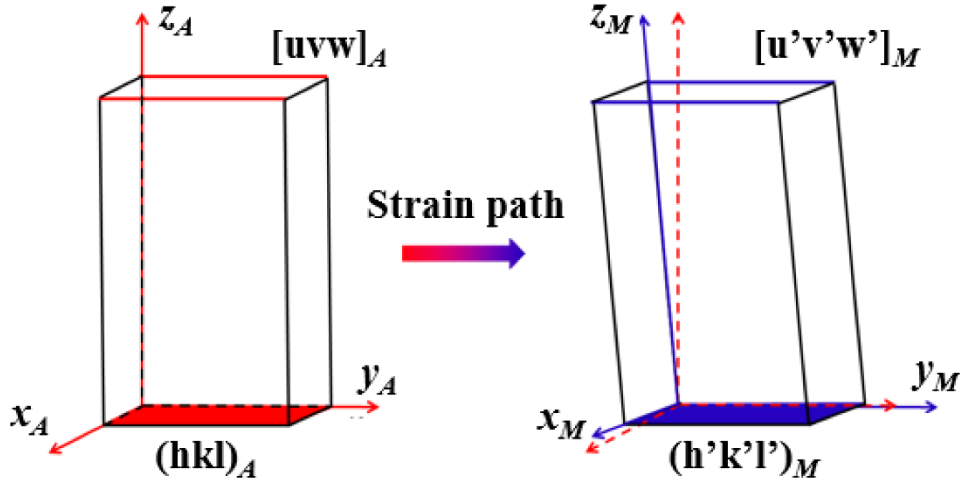


Fig. 4 Illustration of lattice deformation during martensitic transformation under certain transformation orientation relationship (OR).

According to the definition of F , the diagonal elements ε_{ii} represents the normal strain component in the direction of i , and the off-diagonal elements ε_{ij} represent the shear strain component in the direction of i and on the plane normal to the direction of j . We can see from Eqs. (1) and (2) that the lattice deformation under these two ORs is mainly realized by a shear on the corresponding OR system, as highlighted in bold in Eqs. (1) and (2) (0.1002 on the $\{111\}_A$ plane and in the $\langle 110 \rangle_A$ direction for the K–S OR and -0.1312 on the $\{110\}_A$ plane and in the $\langle \bar{1}10 \rangle_A$ direction under the Pitsch OR), accompanied by the other small structural distortion. Clearly, the OR system functions as the deformation system and represents the strain path. If comparing the corresponding values in the two F , one can find that both the normal

strain components (ϵ_{ii}) and the shear strain components (ϵ_{ij}) are comparable in magnitude for the two paths. With the above quantitative information, the temporal evolutions of the structural change following the respective two paths from the parent austenite to the product martensite were calculated and displayed in Fig. 5. It is seen that by the two paths the transformation can be realized independently and arrives at the same final structure. However, under the two paths, the structure deformation happens on different systems, thus they should have different impacts on variant organization. Therefore, the identification of the true paths could be made by the microstructural fingerprints, *i.e.*, the organization of the martensite variants.

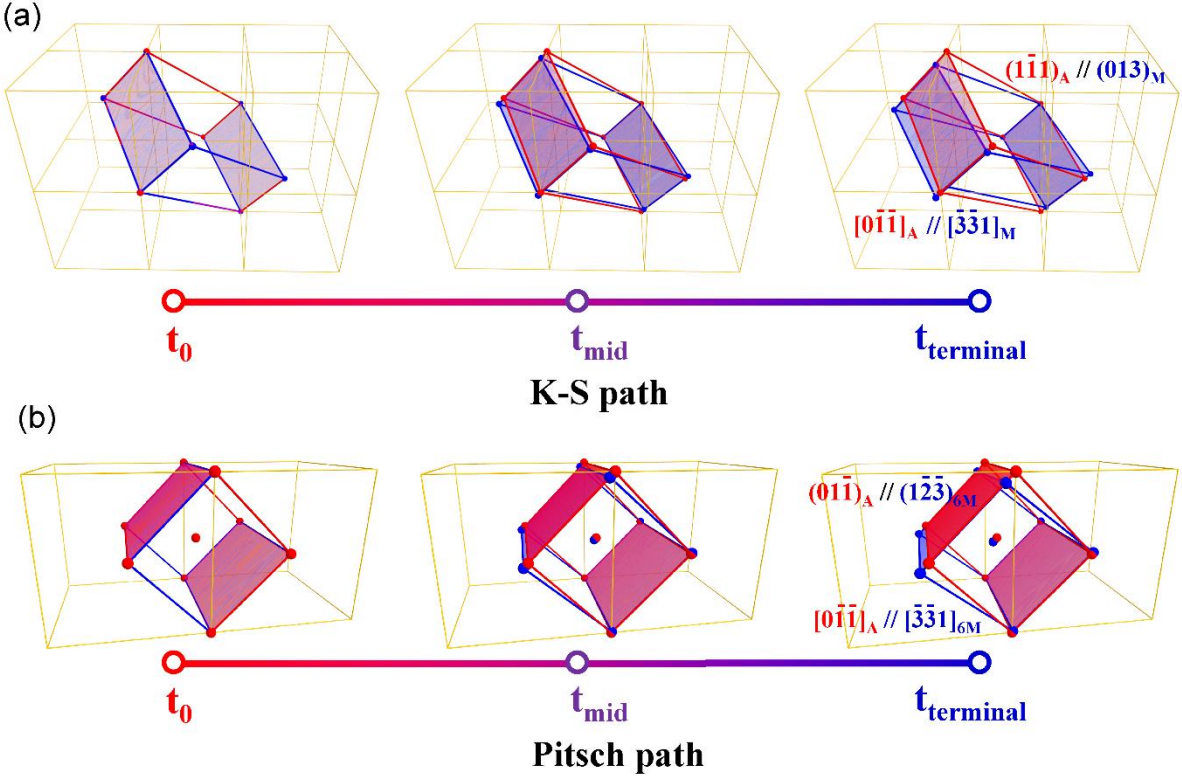


Fig. 5 Illustration of the lattice deformation during martensitic transformation under the K–S (a) and the Pitsch (b) paths. The OR plane and in-plane OR direction parallelism for the austenite and the martensite are depicted by the red and the blue color, respectively. t_0 , t_{mid} and $t_{terminal}$ indicate the initial, the middle and the final temporal stage of transformation.

3.3 Microstructure prediction and verification

As mentioned above, the K–S and the Pitsch paths possess the common transformation direction $\langle \bar{1}10 \rangle_A$ but different transformation planes (Fig. 3b), *i.e.*, $\{111\}_A$ for the K–S path and $\{110\}_A$ for the Pitsch path. Since the transformation planes of these two paths have different crystallographic symmetries, *i.e.*, three-fold for the K–S path ($\{111\}_A$) and two-fold for the Pitsch path $\{110\}_A$, their correlated microstructure features of the low-symmetry phase (martensite) should be different. Thus, we analyzed the variant organization configuration under these two paths.

3.3.1 Martensite variants and their related strain paths under the K–S and the Pitsch paths

The number and the orientation of all possible martensite variants under the K–S and the Pitsch paths were calculated first. The details of the calculation are given in Appendix B. Here, the Bravais lattice frame of the austenite is used as the reference frame. The determined martensite variants under the K–S and the Pitsch paths, henceforth termed as the K–S and the Pitsch variants, are shown in Fig. 6a with the $\langle 001 \rangle_M$ stereographic projection. We see that one austenite can maximally generate 24 variants (labeled as 1 ~ 24) for both the K–S and the Pitsch paths. This is consistent with our experimental result (Fig. 1b). We see from Fig. 6a that the orientations of the 24 K–S variants are almost identical to the 24 Pitsch variants, which is in accordance with the above OR analyses (Fig. 3a). In Table 2, we listed the individual transformation path and the corresponding symmetry operation for all the K–S and the Pitsch variants. Clearly, the K–S and the Pitsch variants with the similar orientations, such as the K–S variant 1 and the Pitsch variant 1 (Fig. 6a), have exactly the same transformation direction

$[10\bar{1}]_A$ but different transformation planes, *i.e.*, the $(\bar{1}\bar{1}\bar{1})_A$ for the K–S variant 1 and the $(101)_A$ for the Pitsch variant 1. Thus, the different impacts of the K–S and the Pitsch transformation path on variant organization should be mainly from the transformation plane.

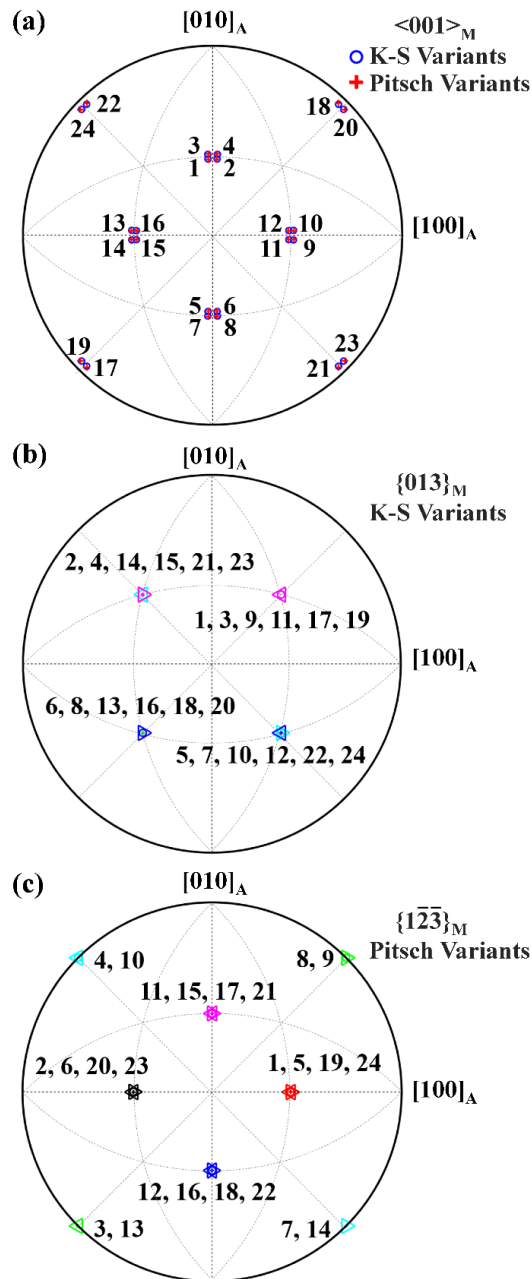


Fig. 6 Stereographic projections of martensite variants under the K–S and the Pitsch paths. (a) $\langle 001 \rangle_M$ pole figure for the K–S and the Pitsch variants; (b) $\{013\}_M$ pole figure for the K–S variants; (c) $\{1\bar{2}\bar{3}\}_M$ pole figure for the Pitsch variants. $(001)_A$ of austenite is utilized as the projection plane.

Table 2 Individual transformation paths and their related rotational symmetry elements for all the 24 martensite variants under the K–S and the Pitsch paths. The expression of crystal symmetry follows the notation used in Ref. [46].

Variant label	Rotation symmetry	K–S path		Pitsch path	
		Transformation plane (TP)	Transformation vector (TV)	Transformation plane (TP)	Transformation vector (TV)
1	(x, y, z)	$(\bar{1} \bar{1} \bar{1})_A$	$[1 0 \bar{1}]_A$	$(1 0 1)_A$	$[1 0 \bar{1}]_A$
2	(x, -y, -z)	$(\bar{1} 1 1)_A$	$[1 0 1]_A$	$(1 0 \bar{1})_A$	$[1 0 1]_A$
3	(-x, -z, -y)	$(1 1 1)_A$	$[\bar{1} 1 0]_A$	$(\bar{1} \bar{1} 0)_A$	$[\bar{1} 1 0]_A$
4	(-x, z, y)	$(1 \bar{1} \bar{1})_A$	$[\bar{1} \bar{1} 0]_A$	$(\bar{1} 1 0)_A$	$[\bar{1} \bar{1} 0]_A$
5	(-x, y, -z)	$(1 \bar{1} 1)_A$	$[\bar{1} 0 1]_A$	$(\bar{1} 0 \bar{1})_A$	$[\bar{1} 0 1]_A$
6	(-x, -y, z)	$(1 1 \bar{1})_A$	$[\bar{1} 0 \bar{1}]_A$	$(\bar{1} 0 1)_A$	$[\bar{1} 0 \bar{1}]_A$
7	(x, -z, y)	$(\bar{1} 1 \bar{1})_A$	$[1 1 0]_A$	$(1 \bar{1} 0)_A$	$[1 1 0]_A$
8	(x, z, -y)	$(\bar{1} \bar{1} 1)_A$	$[1 \bar{1} 0]_A$	$(1 1 0)_A$	$[1 \bar{1} 0]_A$
9	(z, x, y)	$(\bar{1} \bar{1} \bar{1})_A$	$[\bar{1} 1 0]_A$	$(1 1 0)_A$	$[\bar{1} 1 0]_A$
10	(-z, x, -y)	$(1 \bar{1} 1)_A$	$[1 1 0]_A$	$(\bar{1} 1 0)_A$	$[1 1 0]_A$
11	(-y, -x, -z)	$(1 1 1)_A$	$[0 \bar{1} 1]_A$	$(0 \bar{1} \bar{1})_A$	$[0 \bar{1} 1]_A$
12	(y, -x, z)	$(\bar{1} 1 \bar{1})_A$	$[0 \bar{1} \bar{1}]_A$	$(0 \bar{1} 1)_A$	$[0 \bar{1} \bar{1}]_A$
13	(-z, -x, y)	$(1 1 1)_A$	$[1 \bar{1} 0]_A$	$(\bar{1} \bar{1} 0)_A$	$[1 \bar{1} 0]_A$
14	(z, -x, -y)	$(\bar{1} 1 1)_A$	$[\bar{1} \bar{1} 0]_A$	$(1 \bar{1} 0)_A$	$[\bar{1} \bar{1} 0]_A$
15	(-y, x, z)	$(1 \bar{1} \bar{1})_A$	$[0 1 \bar{1}]_A$	$(0 1 1)_A$	$[0 1 \bar{1}]_A$
16	(y, x, -z)	$(\bar{1} \bar{1} 1)_A$	$[0 1 1]_A$	$(0 1 \bar{1})_A$	$[0 1 1]_A$
17	(y, z, x)	$(\bar{1} \bar{1} \bar{1})_A$	$[0 \bar{1} 1]_A$	$(0 1 1)_A$	$[0 \bar{1} 1]_A$
18	(-y, -z, x)	$(1 1 \bar{1})_A$	$[0 1 1]_A$	$(0 \bar{1} 1)_A$	$[0 1 1]_A$
19	(-z, -y, -x)	$(1 1 1)_A$	$[1 0 \bar{1}]_A$	$(\bar{1} 0 \bar{1})_A$	$[1 0 \bar{1}]_A$
20	(z, y, -x)	$(\bar{1} \bar{1} 1)_A$	$[\bar{1} 0 \bar{1}]_A$	$(1 0 \bar{1})_A$	$[\bar{1} 0 \bar{1}]_A$
21	(y, -z, -x)	$(\bar{1} 1 1)_A$	$[0 1 \bar{1}]_A$	$(0 \bar{1} \bar{1})_A$	$[0 1 \bar{1}]_A$
22	(-y, z, -x)	$(1 \bar{1} 1)_A$	$[0 \bar{1} \bar{1}]_A$	$(0 1 \bar{1})_A$	$[0 \bar{1} \bar{1}]_A$
23	(-z, y, x)	$(1 \bar{1} \bar{1})_A$	$[1 0 1]_A$	$(\bar{1} 0 1)_A$	$[1 0 1]_A$
24	(z, -y, x)	$(\bar{1} 1 \bar{1})_A$	$[\bar{1} 0 1]_A$	$(1 0 1)_A$	$[\bar{1} 0 1]_A$

In Figs. 6b and c, we show the stereographic projections of the OR plane, *i.e.*, $\{013\}_M$ of the K–S path and $\{\bar{1}\bar{2}\bar{3}\}_M$ of the Pitsch path, for all the theoretical K–S and Pitsch variants. We see from Fig. 6b that the 24 K–S variants gather into four clusters, each containing 6 variants. The projections of the OR planes of the K–S variants in each cluster exactly overlap with one $\{111\}_A$ pole of austenite, *i.e.*, the pole of transformation plane of the K–S path. Therefore, one transformation plane under the K–S path is associated with 6 martensite variants. As for the Pitsch path, as seen in Fig. 6c, the 24 variants gather into 6 clusters, each containing 4 variants. The Pitsch variants in each cluster share one $\{110\}_A$ plane of austenite, *i.e.*, the transformation plane of the Pitsch path.

In Figs. 7 a₁ and a₂, we plot all transformation directions in one transformation plane for the K–S and the Pitsch paths to clarify the relation of the strain paths for martensite variants generated by the same transformation plane. The green and the red arrows indicate the respective normal direction of the transformation plane and the transformation direction. We see from Fig. 7 a₁ that there exist three physically distinct transformation directions, for example $[10\bar{1}]_A$, $[\bar{1}10]_A$ and $[0\bar{1}1]_A$, on one transformation plane under the K–S path. As for the Pitsch path, as seen in Fig. 7a₂, each transformation plane has only one transformation direction. As revealed above, one transformation plane under the K–S and the Pitsch path can provide 6 and 4 variants. For clarify, in Figs. 7 b and c, we display the individual paths for the 6 $(111)_A$ plane related K–S variants (1, 3, 9, 11, 17 and 19) and the 4 $(10\bar{1})_A$ plane related Pitsch variants (2, 6, 20 and 23). We see from Fig. 7b that for the K–S path one transformation plane and one direction are associated with 2 variants, for example, $[10\bar{1}]_A$ of the austenite can generate the K–S variants 1 (Fig. 7b₁) and 19 (Fig. 7b₄). For these two variants, the sign of the normal of the

transformation plane is changed. Thus, three transformation directions combined with one transformation plane can totally generate 6 variants under the K–S path. For the Pitsch path, as seen in Fig. 7c, one transformation plane is associated with 4 variants. For these variants, both the signs of the transformation plane and direction are changed. For instance, $[101]_A$ direction on $(10\bar{1})_A$ plane can produce variants 2 (Fig. 7c₁), 6 (Fig. 7c₂), 20 (Fig. 7c₃) and 23 (Fig. 7c₄). This difference for the K–S and the Pitsch paths should result in the different variant organization, as depicted next.

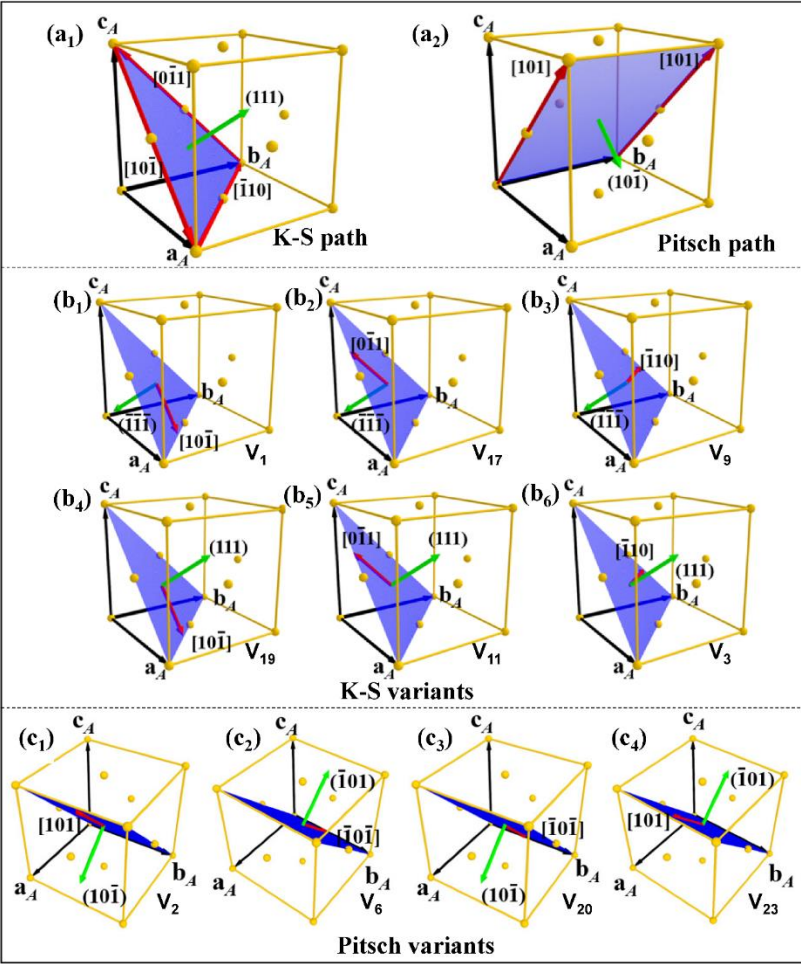


Fig. 7 Illustrations for (a₁) the K–S and (a₂) the Pitsch path. Individual transformation path for (b) the 6 $(111)_A$ plane related K–S variants and (c) the 4 $(10\bar{1})_A$ plane related Pitsch variants. (b₁) ~ (b₆) represent the K–S variants 1, 17, 9, 19, 11 and 3, and (c₁) ~ (c₄) the Pitsch variants 2, 6, 20 and 23.

3.3.2 Different variant combinations under the K–S and the Pitsch paths

We now derive the theoretical characters of martensite microstructure, particularly the variant organization, under the K–S and the Pitsch paths based on the criteria of the minimum elastic strain and interfacial energies. It is known that the microstructure evolution during martensitic transformation is involved in a self-accommodated process to minimize the transformation strain [47]. The self-organized martensite variants should simultaneously satisfy the strain and the stress compatibility conditions [48, 49]. The former guarantees that the microstructure after the structural transition is continuous, and no crack nucleates at the interface between the adjacent variants. The latter ensures that the stress in the vicinity of the interface varies continuously and no stress concentration occurs. For the present material, the transformation started from the nucleation of groups of martensite variants (Fig. 1a). The satisfaction of these two conditions requires that the adjacent two self-accommodated variants are transformed from the same strain path plane and direction of austenite, meaning that the spatially adjacent variants should share the same transformation plane and the same in-plane direction during the nucleation process. For the K–S path, since one transformation plane and direction are associated with only two variants, a sandwich microstructure with alternatively distributed two variants should be energetically favorable in terms of transformation strain compatibility. For the Pitsch path, as one transformation plane and in-plane direction is associated with 4 variants, the microstructure should be composed of groups of 4 co-transformation plane variants.

The co-plane variant group should also possess the minimum interfacial energy between variants and minimum volume elastic strain (from volume misfit) between austenite and variant

group. Here, the possible combinations for martensite variants generated by one transformation plane, e.g., 6 $(111)_A$ plane related K–S variants (Fig. 7b) and 4 $(10\bar{1})_A$ plane related Pitsch variants (Fig. 7c), are discussed. Firstly, the interfacial energy between variants is analyzed by examining their crystallographic orientation relationship [50-52]. For the K–S path, among the 6 co-transformation plane variants, not all 6 variants can be interrelated with twin relations. Only 3 variants can each establish a twin relation with a fourth variant, *i.e.*, variant pairs 3: 1 ($K_1=(\overline{0.0200} \ 0.1204 \ 2.1552)_M, \eta_1=[5.7765 \ \overline{0.1929} \ 0.0643]_M$ or $K_1=(\overline{3.1125} \ 0.1704 \ 0.0207)_M, \eta_1=[\overline{0.0342} \ \overline{0.1251} \ \overline{4.1157}]_M$), 11: 1 ($K_1=(\overline{0.5349} \ \overline{0.9374} \ \overline{1.4130})_M, \eta_1=[\overline{2.7804} \ 3.1890 \ \overline{1.0630}]_M$ or $K_1=(0.4702 \ \overline{0.9396} \ 1.5957)_M, \eta_1=[3.1230 \ 3.1818 \ 0.9532]_M$) and 19: 1 (the type-II twin). Therefore, the boundaries between these variant pairs could be the so-called invariant twinning plane K_1 [50, 53], *i.e.*, the low-energy interface. By contrast, the boundaries for variant pairs 1: 9 and 1: 17 can only be non-coherent high energy boundaries. Consequently, for the K–S path, 3 pairs of twin-related variant combinations (3 individual sandwiches) are favorable in view of interfacial energy. It should be noted that the first two types of twins between variant pairs 3: 1 and 11: 1 have never been experimentally found in the Ni-Mn based alloys. However, for the Pitsch path, all 4 co-transformation plane variants are twin related one another. Thus, all these 4 variants could be interconnected by low-energy coherent interfaces, *i.e.*, the twinning plane.

Apart from interfacial energy, the volume elastic strain for the combinations of the twin-related variants under the K–S and the Pitsch path is evaluated. As is known, both the volume and the shape changes of the martensite nucleus play important roles in the elastic strain energy during martensitic transformation. The total deformation of a twin related variant pair can be

expressed by the following equation:

$$\mathbf{F} = x \times \mathbf{F}_i + (1-x) \times \mathbf{F}_j \quad (0 \leq x \leq 1), \quad (3)$$

where \mathbf{F}_i and \mathbf{F}_j are the deformation gradient tensor of variant i and j , and x is the relative volume fraction of variant i . The three eigenvalues λ_1, λ_2 and λ_3 of \mathbf{F} demonstrate the dimension change in the corresponding eigenvector directions and thus can be used as a measure of volume change and shape change of the twin pair. The values larger than 1 mean elongation and the ones less than 1 mean contraction. If they are all close to 1, it means that the volume of the variant pair is very close to the volume of the initial austenite.

The evolution of the eigenvalues of \mathbf{F} for the combination of the twin-related variant pairs under the K–S and the Pitsch paths are calculated and shown in Figs. 8 a and b. For the K–S path, we can see that for variant pairs 1: 3 and 1: 11 λ_2 and λ_3 vary with the relative volume fraction of the two variants and are very different from 1, although λ_1 is constant. The maximum change happens when the two variants possess an equal volume. This suggests that the formation of such variant pairs create large volume and shape change, and thus large volume misfit between the initial austenite and the formed martensite variant pair. Therefore, such combinations are not energetically favorable. For the combination of variants 1 and 19, we can find that all λ_1, λ_2 and λ_3 equal to those of the single variant 1 or 19 and stay constant with the variation of the volume fraction (Fig. 8a₃). As a result, for the K–S path, among the 6 co-transformation plane variants only one variant pair produces the smallest volume misfit between austenite and martensite and hence is favorable in terms of elastic strain energy. The variants in this pair are also twin related. Thus, under the K–S path, it prefers to form a “sandwich-like” structure with two alternately distributed variants (AB...AB), as illustrated in

Fig. 9a. In contrast, for the Pitsch path, the three eigenvalues of the combined F for all possible variant pairs stay constant with the variation of volume fraction (Fig. 8b). Therefore, one variant can freely organize with any other co-plane variants. The volume change involved is always the smallest. Consequently, the Pitsch path can bring about the self-accommodated 4 alternately distributed variants in a local region of an austenite grain, as illustrated in Fig. 9b.

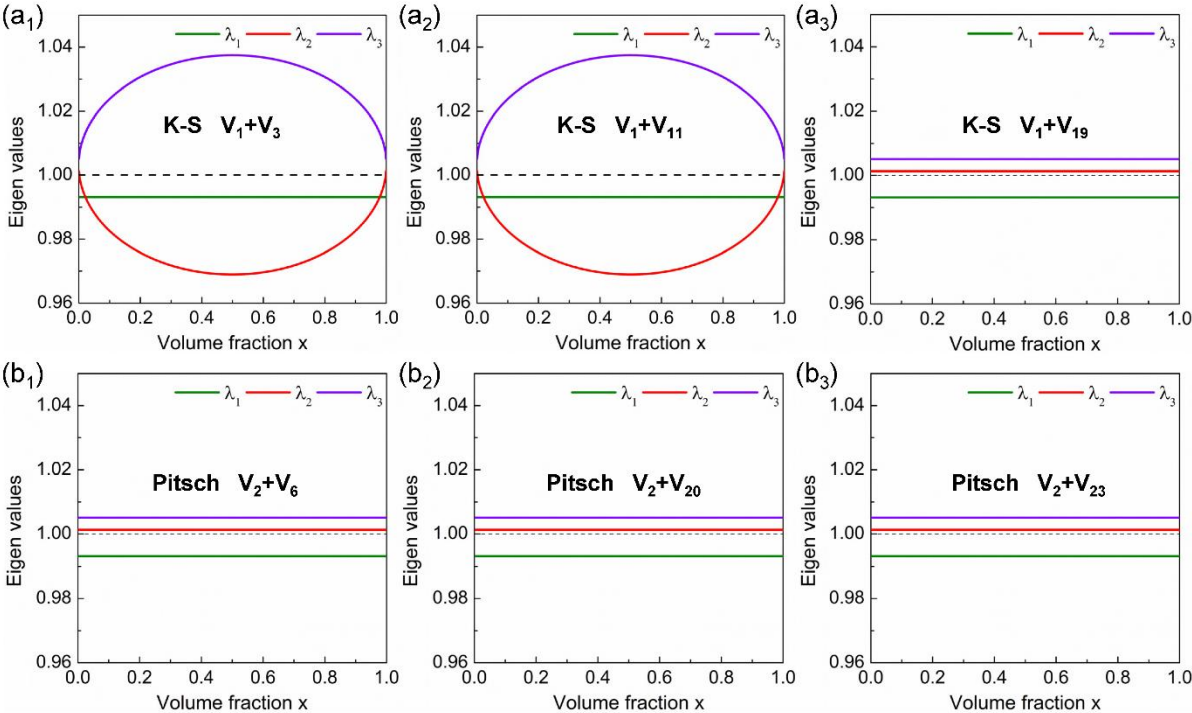


Fig. 8 Eigenvalues λ_1 , λ_2 and λ_3 of the combined deformation gradient tensor for twin-related variant pairs under (a) the K–S and (b) the Pitsch path as a function of relative volume fraction x . (a₁) the K–S variants 1 and 3; (a₂) the K–S variants 1 and 11; (a₃) the K–S variants 1 and 19; (b₁) the Pitsch variants 2 and 6; (b₂) the Pitsch variants 2 and 20; (b₃) the Pitsch variants 2 and 23.

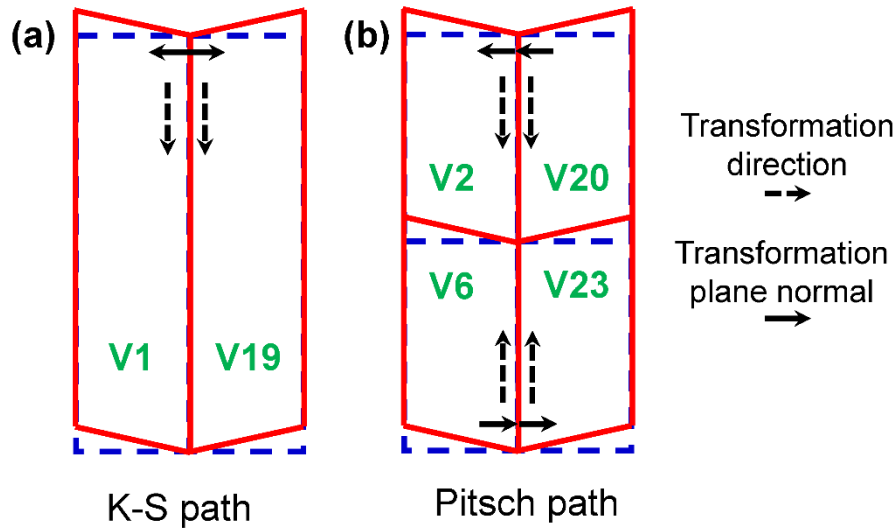


Fig. 9 Theoretical variant organization under (a) the K–S and (b) the Pitsch path.

3.3.3 Comparison of experimental and theoretical variant organization

The above theoretical analyses demonstrate that the different transformation paths result in different compatible variant organizations. For the K–S path, a sandwich structured variant group with two twin-related variants should be formed (Fig. 9a), whereas, for the Pitsch path, a cluster of 4 inter twin-related variants should be produced by the transformation (Fig. 9b). Thus, by comparing the predicted variant organization under the two paths with the observed one, the transformation path for the studied Ni–Mn–In alloys can be uniquely determined. As displayed in Fig. 1a and reported in Refs. [39, 54], the martensite variant group or cluster of the modulated martensite in the Ni–Mn–In alloys is self-organized with 4 twin-related variants rather than 2. In Fig. 10, we plot the $\langle 001 \rangle_M$ stereographic projection of the 4 measured martensite variants in G1 in Fig. 1a and the $\langle 001 \rangle_M$ pole figures for their corresponding theoretical Pitsch variants. We see that the measured variants A, B, C and D are in exact coincidence with the respective theoretical Pitsch variants 19, 5, 1 and 24. This result suggests that the Pitsch path is the strain path of the formation of the studied 6M modulated martensite

in Ni–Mn–In polycrystalline alloys. It should be noted that for the other Ni–Mn-based alloys with different transformation ORs, the transformation strain paths could be different and the martensite variant group configurations could also be different [55, 56].

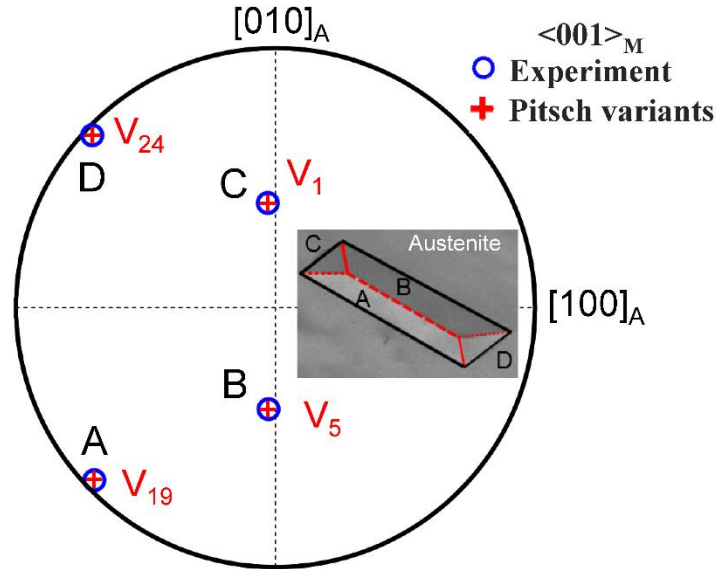


Fig. 10 Comparison of the orientations of the measured martensite variants (blue circles) with the theoretical ones (red crosses) generated through the Pitsch path with the stereographic projection of $\langle 001 \rangle_M$ poles. The inset shows the microstructure of the measured 4 self-organized martensite variants A, B, C and D from G1 in Fig. 1a.

As seen in Fig. 6c and Table 2, these 4 variants are associated with the same Pitsch-type transformation system, *i.e.*, $(1\ 0\ 1)_A[1\ 0\ \bar{1}]_A$, which is in excellent agreement with the above theoretical analyses. In total, there are 6 distinct Pitsch-type transformation planes $\langle 1\ 0\ \bar{1} \rangle_A$ for cubic crystals. Thus, theoretically, one austenite can maximally generate 6 independent martensite groups. This is also in excellent accordance with our experimental observation in Fig. 1b. Furthermore, based on the indirect two-trace method [57] to determine the interface plane, we find that the Miller indices of the interface plane between variants A: C (or B: D) are $\{\bar{1}\bar{2}\bar{3}\}_M$. The interface plane is exactly parallel to the $\{101\}_A$ plane of austenite, *i.e.*, the transformation plane of the Pitsch path. However, no variant interface planes are in coincidence

with the $\{013\}_M$ plane that corresponds to the transformation plane of the K–S path. Thus, for the modulated Ni–Mn–In martensite, the Pitsch path is indeed the physical transformation strain path. The mutual satisfaction of the K–S OR by the parent austenite and the product martensite in the studied Ni–Mn based alloys should be a geometrical coincidence. This results from the specific crystal structure systems and the particular lattice parameters of the two end phases of the transformation.

4. Conclusions

In this work, the ambiguous K–S $\{111\}_A \langle \bar{1}10 \rangle_A$ and Pitsch $\{110\}_A \langle \bar{1}10 \rangle_A$ transformation paths for the Ni–Mn-based alloys with modulated martensite were comprehensively investigated by means of experimental examinations using SEM-EBSD and theoretical analyses in the frame of crystallographic theory. The main conclusions can be drawn as follows:

(1) The modulated martensite of Ni–Mn-based alloys has a self-accommodated microstructure grouped with four inter twin-related martensite variants. The K–S and the Pitsch ORs are mutually respected by the parent and the product phase. Under the two ORs, the OR plane and the OR direction is associated with the major strain component and the OR system is physically the transformation strain path.

(2) Crystallographic analyses showed that by satisfying the strain and stress compatibility condition and the minimum energy criteria, theoretically, the K–S path produces 2 variants as a self-accommodated variant group, whereas the Pitsch path produces 4 variants as a self-accommodated variant group.

(3) Supported with the experimental results, the Pitsch path is the energetically favorable

transformation path and actually occurs in stress-free austenite of the Ni–Mn based alloys.

The present results shed new light on the physical process of the martensitic transformation that is associated with multiple functionalities of the Ni–Mn based alloys. The obtained knowledge is useful for the efforts in enhancing the martensitic transformation-related functionalities through reducing transformation resistance. The analyzing scheme, *i.e.*, determination of transformation strain path *via* the microstructure characters of the low-symmetric phase, could be generalized to determine the transformation characters for martensitic transformation, even for other shear dominated solid-state phase transition, in many other alloy systems.

Acknowledgment

This work is supported by the National Natural Science Foundation of China (Grant No. 51801020), the Fundamental Research Funds for the Central Universities (Grant No. N2002005, N2002021), the Liaoning Revitalization Talents Program (Grant No. XLYC1802023), and Programme of Introducing Talents of Discipline Innovation to Universities (the 111 Project of China, No. BP0719037).

Appendix A. Difference of the theoretical and experimental ORs

The experimental crystallographic ORs (Δg^{exp}) can be calculated based on the measured orientations of austenite (g_A) and martensite (g_{6M}) by Eq. A.1.

$$\Delta g^{\text{exp}} = S_i^{-1} \times g_A^{-1} \times g_M \times S_k \quad (\text{A.1})$$

where S_i ($i = 1 \sim 24$) and S_k ($k = 1 \sim 2$) represent the rotational symmetry matrices of the austenite (cubic) and martensite (monoclinic), respectively. The theoretical crystallographic ORs (Δg_0^{OR}) of the Bain, the N–W, the K–S and the Pitsch relations can be calculated on the

basis of the corresponding plane and in-plane parallel pairs and crystal structure information of austenite and martensite, respectively. The determined Δg_0^{OR} , expressed in terms of the Euler angles $(\varphi_1, \Phi, \varphi_2)$ with respect to the austenite lattice reference, is given in [Table 1](#).

The difference between the theoretical and experimental ORs can be evaluated by the rotational difference $\Delta\varepsilon$ between the theoretical Δg_0^{OR} and experimental misorientation Δg^{exp} :

$$\Delta\varepsilon = \Delta g^{\text{exp}} \times S_1^{-1} \times (\Delta g_0^{\text{OR}})^{-1} \times S_j \quad (\text{A.2})$$

where S_j ($j = 1 \sim 24$) and S_1 ($1 = 1 \sim 2$) represent the rotation symmetry matrices of the austenite (cubic) and martensite (monoclinic), respectively. These rotational difference $\Delta\varepsilon$ can also be expressed in terms of rotation angle/axis pairs (ω, \mathbf{d}) . Among 48×48 possible $\Delta\varepsilon$ that are equivalent by symmetry, the one with the minimal ω value can be utilized to characterize the difference between the experimental and theoretical ORs.

Appendix B. Possible martensite variants under certain OR

The crystallographic orientations of possible martensite variants (g_M^i) with respect to the austenite lattice reference under certain OR can be determined by the follow equation:

$$g_M^i = S_A^i \times \Delta g_0^{\text{OR}} \quad (\text{B.1})$$

where S_A^i ($i = 1 \sim 24$) are the rotational symmetry matrices of cubic lattice for the austenite phase. Δg_0^{OR} represent the theoretical OR matrix from the orthonormal basis of austenite lattice to that of martensite lattice. As show in [Eq. B.1](#), the number of martensite orientation matrices equal to the number of the symmetry operators of the austenite lattice. Thus, for a certain OR, it leads to a maximum of 24 variants in the case of a cubic austenite grain. However, due to the possible symmetry of Δg_0^{OR} under certain OR, some variants might coincide in the

orientation space [50], and then the number of the physically distinguishable variants may be less than 24.

References

- [1] R. Kainuma, Y. Imano, W. Ito, Y. Sutou, H. Morito, S. Okamoto, O. Kitakami, K. Oikawa, A. Fujita, T. Kanomata, K. Ishida, Magnetic-field-induced shape recovery by reverse phase transformation, *Nature* 439(7079) (2006) 957-960.
- [2] Y.D. Wang, Y. Ren, H.Q. Li, H. Choo, M.L. Benson, D.W. Brown, P.K. Liaw, L. Zuo, G. Wang, D.E. Brown, E.E. Alp, Tracing memory in polycrystalline ferromagnetic shape-memory alloys, *Adv. Mater.* 18(18) (2006) 2392-2396.
- [3] X. Sun, D. Cong, Y. Ren, K.-D. Liss, D.E. Brown, Z. Ma, S. Hao, W. Xia, Z. Chen, L. Ma, X. Zhao, Z. He, J. Liu, R. Li, Y. Wang, Magnetic-field-induced strain-glass-to-martensite transition in a Fe-Mn-Ga alloy, *Acta Mater.* 183 (2020) 11-23.
- [4] J. Liu, T. Gottschall, K.P. Skokov, J.D. Moore, O. Gutfleisch, Giant magnetocaloric effect driven by structural transitions, *Nat. Mater.* 11(7) (2012) 620-626.
- [5] T. Gottschall, A. Gracia-Condal, M. Fries, A. Taubel, L. Pfeuffer, L. Manosa, A. Planes, K.P. Skokov, O. Gutfleisch, A multicaloric cooling cycle that exploits thermal hysteresis, *Nat. Mater.* 17(10) (2018) 929-934.
- [6] L. Mañosa, D. Gonzalez-Alonso, A. Planes, E. Bonnot, M. Barrio, J.-L. Tamarit, S. Aksoy, M. Acet, Giant solid-state barocaloric effect in the Ni–Mn–In magnetic shape-memory alloy, *Nat. Mater.* 9(6) (2010) 478-481.
- [7] Y.H. Qu, D.Y. Cong, S.H. Li, W.Y. Gui, Z.H. Nie, M.H. Zhang, Y. Ren, Y.D. Wang, Simultaneously achieved large reversible elastocaloric and magnetocaloric effects and their coupling in a magnetic shape memory alloy, *Acta Mater.* 151 (2018) 41-55.
- [8] B. Wang, Y. Liu, P. Ren, B. Xia, K. Ruan, J. Yi, J. Ding, X. Li, L. Wang, Large exchange bias after zero-field cooling from an unmagnetized state, *Phys. Rev. Lett.* 106(7) (2011) 077203.
- [9] V.K. Sharma, M.K. Chattopadhyay, K.H.B. Shaeb, A. Chouhan, S.B. Roy, Large magnetoresistance in Ni₅₀Mn₃₄In₁₆ alloy, *Appl. Phys. Lett.* 89(22) (2006) 222509.

- [10] S.Y. Yu, Z.H. Liu, G.D. Liu, J.L. Chen, Z.X. Cao, G.H. Wu, B. Zhang, X.X. Zhang, Large magnetoresistance in single-crystalline $\text{Ni}_{50}\text{Mn}_{50-x}\text{In}_x$ alloys ($x=14-16$) upon martensitic transformation, *Appl. Phys. Lett.* 89(16) (2006) 162503.
- [11] J. Zhang, Z. Ding, R. Hou, J. Gao, J. Zhu, Giant high temperature superelasticity in $\text{Ni}_{53}\text{Mn}_{24}\text{Ga}_{21}\text{Co}_1\text{Cu}_1$ microwires, *Intermetallics* 122 (2020) 106799.
- [12] H. Chen, Y.D. Wang, Z. Nie, R. Li, D. Cong, W. Liu, F. Ye, Y. Liu, P. Cao, F. Tian, X. Shen, R. Yu, L. Vitos, M. Zhang, S. Li, X. Zhang, H. Zheng, J.F. Mitchell, Y. Ren, Unprecedented non-hysteretic superelasticity of [001]-oriented NiCoFeGa single crystals, *Nat. Mater.* 19(7) (2020) 712-718.
- [13] Z.L. Wang, P. Zheng, Z.H. Nie, Y. Ren, Y.D. Wang, P. Müllner, D.C. Dunand, Superelasticity by reversible variants reorientation in a Ni–Mn–Ga microwire with bamboo grains, *Acta Mater.* 99 (2015) 373-381.
- [14] P. Zhao, C. Shen, J. Li, Y. Wang, Effect of nonlinear and noncollinear transformation strain pathways in phase-field modeling of nucleation and growth during martensite transformation, *NPJ Comput. Mater.* 3(1) (2017) 19.
- [15] C. Lexcelent, P. Blanc, N. Creton, Two ways for predicting the hysteresis minimisation for shape memory alloys, *Mater. Sci. Eng. A* 481 (2008) 334-338.
- [16] M. Gouné, F. Danoix, J. Ågren, Y. Bréchet, C.R. Hutchinson, M. Militzer, G. Purdy, S. van der Zwaag, H. Zurob, Overview of the current issues in austenite to ferrite transformation and the role of migrating interfaces therein for low alloyed steels, *Mater. Sci. Eng. R* 92(0) (2015) 1-38.
- [17] E.C. Bain, N.Y. Dunkirk, The nature of martensite, *Trans. AIME* 70(1) (1924) 25-35.
- [18] A. Ayuela, J. Enkovaara, R.M. Nieminen, Ab initio study of tetragonal variants in Ni_2MnGa alloy, *J. Phys. Condens. Matter* 14(21) (2002) 5325-5336.
- [19] P. Entel, M.E. Gruner, M. Acet, A. Cakir, R. Arroyave, T. Duong, S. Sahoo, S. Fahler, V.V. Sokolovskiy, Properties and Decomposition of Heusler Alloys, *Energy Technol.* 6(8) (2018) 1478-1490.
- [20] L. Mañosa, A. Gonzalez-Comas, E. Obradó, A. Planes, V.A. Chernenko, V.V. Kokorin, E. Cesari, Anomalies related to the TA_2 -phonon-mode condensation in the Heusler Ni_2MnGa alloy, *Phys. Rev. B* 55(17) (1997) 11068-11071.

- [21] P. Entel, A. Dannenberg, M. Siewert, H.C. Herper, M.E. Gruner, D. Comtesse, H.-J. Elmers, M. Kallmayer, Basic Properties of Magnetic Shape-Memory Materials from First-Principles Calculations, *Metall. Mater. Trans. A* 43(8) (2012) 2891-2900.
- [22] C. Bungaro, K.M. Rabe, A. Dal Corso, First-principles study of lattice instabilities in ferromagnetic Ni₂MnGa, *Phys. Rev. B* 68(13) (2003) 134104.
- [23] D.Y. Cong, Y.D. Zhang, Y.D. Wang, M. Humbert, X. Zhao, T. Watanabe, L. Zuo, C. Esling, Experiment and theoretical prediction of martensitic transformation crystallography in a Ni-Mn-Ga ferromagnetic shape memory alloy, *Acta Mater.* 55(14) (2007) 4731-4740.
- [24] C. LExcellent, P. Blanc, Phase transformation yield surface determination for some shape memory alloys, *Acta Mater.* 52(8) (2004) 2317-2324.
- [25] C. LExcellent, *Shape-memory Alloys Handbook*, John Wiley & Sons, Hoboken, 2013.
- [26] D.C. Lagoudas, P.B. Entchev, P. Popov, E. Patoor, L.C. Brinson, X.J. Gao, Shape memory alloys, Part II: Modeling of polycrystals, *Mech. Mater.* 38(5-6) (2006) 430-462.
- [27] E. Patoor, D.C. Lagoudas, P.B. Entchev, L.C. Brinson, X. Gao, Shape memory alloys, Part I: General properties and modeling of single crystals, *Mech. Mater.* 38(5) (2006) 391-429.
- [28] Z. Li, N. Xu, Y. Zhang, C. Esling, J.-M. Raulot, X. Zhao, L. Zuo, Composition-dependent ground state of martensite in Ni–Mn–Ga alloys, *Acta Mater.* 61(10) (2013) 3858-3865.
- [29] J. Pons, V.A. Chernenko, R. Santamarta, E. Cesari, Crystal structure of martensitic phases in Ni–Mn–Ga shape memory alloys, *Acta Mater.* 48(12) (2000) 3027-3038.
- [30] G. Kurdjumov, G. Sachs, Over the mechanisms of steel hardening, *Z. Phys.* 64 (1930) 325-343.
- [31] R.F. Bunshah, R.F. Mehl, Rate of propagation of martensite, *Trans. AIME* 197 (1953) 1251-1258.
- [32] K. Mukherjee, On the dynamics of martensitic transformation, *Trans. TMS-AIME* 242 (1968) 1495-1501.
- [33] Z.B. Li, Y.D. Zhang, C. Esling, X. Zhao, L. Zuo, Determination of the orientation relationship between austenite and incommensurate 7M modulated martensite in Ni-Mn-Ga alloys, *Acta Mater.* 59(7) (2011) 2762-2772.

- [34] Z.B. Li, Y.D. Zhang, C. Esling, X. Zhao, L. Zuo, Determination of the orientation relationship between austenite and 5M modulated martensite in Ni-Mn-Ga alloys, *J. Appl. Cryst.* 44 (2011) 1222-1226.
- [35] C.Y. Zhang, Y.D. Zhang, C. Esling, X. Zhao, L. Zuo, Crystallographic features of the martensitic transformation and their impact on variant organization in the intermetallic compound Ni₅₀Mn₃₈Sb₁₂ studied by SEM/EBSD, *IUCrJ* 4 (2017) 700-709.
- [36] H.-L. Yan, Y. Zhang, N. Xu, A. Senyshyn, H.-G. Brokmeier, C. Esling, X. Zhao, L. Zuo, Crystal structure determination of incommensurate modulated martensite in Ni-Mn-In Heusler alloys, *Acta Mater.* 88 (2015) 375-388.
- [37] H.-L. Yan, C. Zhang, Y. Zhang, X. Wang, C. Esling, X. Zhao, L. Zuo, Crystallographic insights into Ni-Co-Mn-In metamagnetic shape memory alloys, *J. Appl. Cryst.* 49(5) (2016) 1585-1592.
- [38] Y.D. Wang, D.W. Brown, H. Choo, P.K. Liaw, D.Y. Cong, M.L. Benson, L. Zuo, Experimental evidence of stress-field-induced selection of variants in Ni-Mn-Ga ferromagnetic shape-memory alloys, *Phys. Rev. B* 75(17) (2007) 174404.
- [39] H.-L. Yan, B. Yang, Y.D. Zhang, Z.B. Li, C. Esling, X. Zhao, L. Zuo, Variant organization and mechanical detwinning of modulated martensite in Ni-Mn-In metamagnetic shape-memory alloys, *Acta Mater.* 111 (2016) 75-84.
- [40] Z. Nishiyama, X-ray investigation of the mechanism of the transformation from face-centered cubic lattice to body-centered cubic, *Sci. Rep.* 23 (1934) 637-664.
- [41] G. Wassermann, K. Mitt, About the mechanism of α - γ transformation of the iron, *Inst. Eisenforsch.* 17 (1935) 149-155.
- [42] W. Pitsch, Der orientierungszusammenhang zwischen zementit und austenit, *Acta Metall.* 10(9) (1962) 897-900.
- [43] C.Q. Lin, Crystallographic study on Ni-Mn-Sn metamagnetic shape memory alloys, Université de Lorraine, 2017.
- [44] S. Van Smaalen, Incommensurate crystallography, Oxford University Press, Oxford, 2007.
- [45] B. Yang, Fabrication and crystallographic features of epitaxial NiMnGa ferromagnetic shape memory alloy thin films, Université de Lorraine, 2014.

- [46] M. Humbert, F. Wagner, C. Esling, Numbering the crystallographic variants in phase transformation, *J. Appl. Cryst.* 25(6) (1992) 724-730.
- [47] K. Bhattacharya, Self-accommodation in martensite, *Arch. Ration. Mech. Anal.* 120(3) (1992) 201-244.
- [48] E. Patoor, A. Eberhardt, M. Berveiller, Micromechanical modelling of superelasticity in shape memory alloys, *J. Phys. IV* 6(C1) (1996) 277-292.
- [49] Y. Chemisky, A. Duval, E. Patoor, T. Ben Zineb, Constitutive model for shape memory alloys including phase transformation, martensitic reorientation and twins accommodation, *Mech. Mater.* 43(7) (2011) 361-376.
- [50] Y.D. Zhang, Z.B. Li, C. Esling, J. Muller, X. Zhao, L. Zuo, A general method to determine twinning elements, *J. Appl. Cryst.* 43 (2010) 1426-1430.
- [51] I.J. Beyerlein, J. Wang, M.R. Barnett, C.N. Tome, Double twinning mechanisms in magnesium alloys via dissociation of lattice dislocations, *Proc. R. Soc. A-Math. Phys. Eng. Sci.* 468(2141) (2012) 1496-1520.
- [52] D.Y. Cong, Y.D. Zhang, Y.D. Wang, C. Esling, X. Zhao, L. Zuo, Determination of microstructure and twinning relationship between martensitic variants in 53 at.%Ni-25 at.%Mn-22 at.%Ga ferromagnetic shape memory alloy, *J. Appl. Cryst.* 39 (2006) 723-727.
- [53] I. Beyerlein, X. Zhang, A. Misra, Growth twins and deformation twins in metals, *Annu. Rev. Mater. Res.* 44(1) (2014) 329-363.
- [54] Z.B. Li, Y.D. Zhang, C. Esling, X. Zhao, L. Zuo, Evidence for a monoclinic incommensurate superstructure in modulated martensite, *Acta Mater.* 60(20) (2012) 6982-6990.
- [55] R. Chulist, M. Faryna, M.J. Szczerba, Orientation relationship between austenite and non-modulated martensite in Ni–Mn–Ga single crystals, *Acta Mater.* 103 (2016) 836-843.
- [56] D.Y. Cong, Y.D. Zhang, C. Esling, Y.D. Wang, J.S. Lecomte, X. Zhao, L. Zuo, Microstructural and crystallographic characteristics of interpenetrating and non-interpenetrating multiply twinned nanostructure in a Ni-Mn-Ga ferromagnetic shape memory alloy, *Acta Mater.* 59(18) (2011) 7070-7081.
- [57] Y.D. Zhang, C. Esling, X. Zhao, L. Zuo, Indirect two-trace method to determine a faceted low-energy interface between two crystallographically correlated crystals, *J. Appl. Cryst.* 40

(2007) 436-440.

Figure captions:

Fig. 1 Phase indexed (a₁) and orientation (a₂) micrographs of the dual-phase Ni₄₅Co₅Mn_{36.8}In_{13.2} alloy. The solid black lines indicate the phase boundaries between austenite and martensite. The red dotted, red dashed and red solid lines represent the type-I, type-II and compound twin interfaces. Crystallographic orientation (b₁) and band quality indexed (b₂) micrograph of the single martensite of Ni₂Mn_{1.44}In_{0.56} alloy. The solid black lines represent the initial austenite grain boundaries. G1 to G6 indicate the distinct martensite groups.

Fig. 2 Illustrations of lattice correspondences between the austenite and the martensite under the Bain (a), the Pitsch (b), the K–S (c) and the N–W (d) OR. The crystal lattices of the austenite and the martensite are indicated in red and blue, respectively. Subscripts “A” and “M” represent austenite and martensite, respectively.

Fig. 3 (a) Orientations of martensite lattices under the K–S (blue) and the Pitsch (green) relation. (b) Stereographic projection of the OR planes and the OR directions for the K–S and the Pitsch OR in the lattice frame of austenite.

Fig. 4 Illustration of lattice deformation during martensitic transformation under certain transformation orientation relationship (OR).

Fig. 5 Illustration of the lattice deformation during martensitic transformation under the K–S (a) and the Pitsch (b) paths. The OR plane and in-plane OR direction parallelism for the austenite and the martensite are depicted by the red and the blue color, respectively. t_0 , t_{mid} and $t_{terminal}$ indicate the initial, the middle and the final temporal stage of transformation.

Fig. 6 Stereographic projections of martensite variants under the K–S and the Pitsch path. (a) $\langle 001 \rangle_M$ pole figure for the K–S and the Pitsch variants; (b) $\{013\}_M$ pole figure for the K–S variants; (c) $\{1\bar{2}\bar{3}\}_M$ pole figure for the Pitsch variants. $(001)_A$ of austenite is utilized as the projection plane.

Fig. 7 Illustrations for (a₁) the K–S and (a₂) the Pitsch path. Individual transformation path for (b) the 6 $(111)_A$ plane related K–S variants and (c) the 4 $(10\bar{1})_A$ plane related Pitsch variants.

(b₁) ~ (b₆) represent the K–S variants 1, 17, 9, 19, 11 and 3, and (c₁) ~ (c₄) the Pitsch variants 2, 6, 20 and 23.

Fig. 8 Eigenvalues λ_1 , λ_2 and λ_3 of the combined deformation gradient tensor for twin-related variant pairs under (a) the K–S and (b) the Pitsch path as a function of relative volume fraction x . (a₁) the K–S variants 1 and 3; (a₂) the K–S variants 1 and 11; (a₃) the K–S variants 1 and 19; (b₁) the Pitsch variants 2 and 6; (b₂) the Pitsch variants 2 and 20; (b₃) the Pitsch variants 2 and 23.

Fig. 9 Theoretical variant organization under (a) the K–S and (b) the Pitsch path.

Fig. 10 Comparison of the orientations of the measured martensite variants (blue circles) with the theoretical ones (red crosses) generated through the Pitsch path with the stereographic projection of $\langle 001 \rangle_M$ poles. The inset shows the microstructure of the measured 4 self-organized martensite variants A, B, C and D from G1 in Fig. 1a.